

# Materials Genomics Search for Possible Helium-Absorbing Nano-Phases in Fusion Structural Materials

Haowei Xu, So Yeon Kim, Di Chen, Jean-Phillippe Monchoux, Thomas Voisin, Cheng Sun,\* and Ju Li\*

Civilian fusion demands structural materials that can withstand the harsh environments imposed inside fusion plasma reactors. The structural materials often transmute under 14.1 MeV fast neutrons, producing helium (He), which embrittles the grain boundary (GB) network. Here, it is shown that neutron-friendly and mechanically strong nano-phases with atomic-scale free volume can have low He-embedding energy  $\mathcal{E}_{\text{emb}}$  and  $>10$  at.% He-absorbing capacity, and can be especially advantageous for soaking up He on top of resisting radiation damage and creep, provided they have thermodynamic compatibility with the matrix phase, satisfactory equilibrium wetting angle, as well as a high enough melting point. The preliminary experimental demonstration proves that  $\mathcal{E}_{\text{emb}}$  is a good ab initio predictor of He shielding potency in nano-heterophase materials, and thus,  $\mathcal{E}_{\text{emb}}$  is used as a key feature for computational screening. In this context, a list of viable compounds expected to be good He-absorbing nano-phases is presented, taking into account  $\mathcal{E}_{\text{emb}}$ , the neutron absorption and activation cross-sections, the elastic moduli, melting temperature, the thermodynamic compatibility, and the equilibrium wetting angle of the nano-phases with the Fe matrix as an example.

neutrons with kinetic energy as high as 14.1 MeV to impinge on the plasma vessel material. This poses a grand challenge to material scientists, since when bombarded by these high-energy neutrons, transition metals—the primary constituent elements of the materials for structural components—often transmute to produce helium (He).<sup>[1]</sup> Because He is an inert-gas element, it interacts with the matrix atoms in a repulsive manner and thus tends to segregate into grain boundaries (GBs), which can have a somewhat larger free volume than the lattice.<sup>[2]</sup> Once a monolayer of He (coverage of  $\approx 7 \times 10^{14} \text{ cm}^{-2}$  or  $7 \text{ nm}^{-2}$ )<sup>[3]</sup> manages to segregate on a 2D GB, they jack up the metal–metal bonding distances across the GB to be sufficiently extended so that the GB can no longer sustain appreciable tensile or shear load, and would easily debond. To make matters worse, as a 2D GB cannot freely terminate crystallographically, most GBs are not alone but part of a percolating 2D GB network, which forms a natural template for long cracks that are highly

damaging. 2D traction-free openings are the worst form of damage; among spherical, prolate (needle-shaped), and oblate (disk-shaped) cavities in a solid body, the oblate-shaped cavities engender the largest stress amplification factor that tends to infinity when the long-to-short axis ratio turns to infinity,<sup>[4]</sup> thereby self-evolving into a penny-shaped crack. The stress amplification

## 1. Introduction

Ever since harvesting nuclear fission energy for electricity production became a reality in 1957, fusion power has been the dream energy source for terrestrial applications and space explorations. To enable nuclear fusion, it is necessary to allow fast

H. Xu, J. Li  
Department of Nuclear Science and Engineering  
Massachusetts Institute of Technology  
Cambridge, MA 02139, USA  
E-mail: liju@mit.edu


S. Y. Kim, J. Li  
Department of Materials Science and Engineering  
Massachusetts Institute of Technology  
Cambridge, MA 02139, USA

D. Chen  
Department of Physics and Texas Center for Superconductivity  
University of Houston  
Houston, TX 77204, USA

J.-P. Monchoux  
Centre for Materials Elaboration and Structural Studies  
University of Toulouse  
French National Centre for Scientific Research  
Toulouse 31055, France

T. Voisin  
Materials Science Division  
Lawrence Livermore National Laboratory  
Livermore, CA 94550, USA

C. Sun  
Characterization and Advanced PIE Division  
Idaho National Laboratory  
Idaho Falls, ID 83415, USA  
E-mail: cheng.sun@inl.gov

 The ORCID identification number(s) for the author(s) of this article can be found under <https://doi.org/10.1002/advs.202203555>

© 2022 The Authors. Advanced Science published by Wiley-VCH GmbH. This is an open access article under the terms of the Creative Commons Attribution License, which permits use, distribution and reproduction in any medium, provided the original work is properly cited.

DOI: 10.1002/advs.202203555

factors in prolate and spherical cavities, in contrast, stay bounded. GBs are thus naturally less tolerant against damage growth owing to their locally 2D free-volume segregation and globally percolating topology.<sup>[2,5]</sup> By this mechanism, He in structural components can be extremely detrimental even with very low bulk concentration ( $\approx 0.01$  at.%, or 100 appm), if they manage to diffuse to and segregate at the GBs.

In this regard, nanodispersion-strengthened materials, which were originally developed for high-temperature creep-resistance,<sup>[6]</sup> have drawn attention as fusion structural materials with their remarkable radiation resistance (measured in the unit of displacements per atom, dpa) and He tolerance (measured in the unit of atomic ppm of He per matrix atom, appm).<sup>[1,7,8]</sup> In particular, oxide-dispersion-strengthened (ODS) steels have been demonstrated to have tolerance against He-induced embrittlement as well as superior tensile, creep, and fatigue strength at elevated temperatures.<sup>[9]</sup> Transmission electron microscopy (TEM) studies have revealed that He bubbles and voids form preferentially in the close vicinity to the nano-oxide dispersions in ODS steels.<sup>[10]</sup> The phase boundaries (PBs), e.g., oxide-matrix interfaces, can be sinks for He because they are often incoherent interfaces with excess atomic-scale free volume. But unlike the GBs of a polycrystal, PBs wrapping the nanodispersoids are topologically different in that they are isolated and do not form a percolating network, as the second phase volume fraction is often only on the order of 1 vol.%, below the percolation threshold. And thus even when the PB around an isolated nanoparticle becomes fully debonded after radiation, the limited spatial extent of  $\approx 10$  nm of such opening and the sphericity of the nanoparticle mean such an opening around the “0D” nano-phase is much less damaging, with non-singular stress-amplification factor independent of the spherical diameter. The same can be shown for “1D” or needle/wire-like nano-phases—even their complete debonding with the matrix does not lead to singularity in the stress-amplification factor, regardless of the needle orientation with respect to stress. Thus, uniformly dispersed “0D”/“1D” morphology nano-heterophases may screen and shield the GB from He segregation by attracting and soaking up the He inside their own lattices or at the incoherent PBs, if these sites have lower He embedding energy ( $\mathcal{E}_{\text{emb}}$ ) than the percolating matrix GBs. In this work, we propose that by dispersing nanoparticles or nanowires of secondary phases (that may not be limited to oxides but could also be carbides, nitrides, borides, etc.), the lattice interior of such secondary phases may absorb He atoms with significantly lower embedding energy than that of the matrix GB, thereby screening and protecting the matrix GBs from He attack.

For the proposed He-tolerant design, let us first examine some numbers in practice. We note that the engineering requirement is often to tolerate a few thousand appm He—in the fusion reactor material, the appm-to-dpa ratio is typically  $\approx 10$ , thus a desirable fusion structural material should be able to sustain a few hundred dpa radiation damage and a few thousand appm He, at temperatures up to 800 °C. This would allow a few years of service life for the ARC (affordable, robust, compact) power reactor vacuum vessel.<sup>[11]</sup> Previously, we have already demonstrated uniform dispersion of 1D carbide nano-phases at up to 2 vol.% can greatly improve room-temperature tensile strength as well as high-temperature creep strength without sacrificing the tensile

ductility.<sup>[5,12,13]</sup> The system also showed superior radiation resistance up to 70 dpa.<sup>[12]</sup> This is attributed to the 1D carbide nano-phases being radiation defect sinks.<sup>[14]</sup> If such uniformly dispersed carbides, oxides, nitrides, phosphides, borides ( $^{11}\text{B}$ ), etc. can also absorb He within their bulk lattices, then even 10 at.% uptakes in the nano-phase lattice should be able to soak up all the He in the matrix and protect the matrix GBs, since a few thousand appm can be accommodated by  $\approx 10$  at.% (uptakes per 2nd phases)  $\times$  2 vol.% (the volume fraction of 2nd phases in a composite), provided that  $\mathcal{E}_{\text{emb}}$  (2nd phase)  $<$   $\mathcal{E}_{\text{emb}}$  (matrix GB) and that the nano-heterophases (probably a few nanometre to  $10^1$  nm in diameter) are uniformly distributed spatially when viewed at a  $10^2$  nm length scale, which needs to be smaller than the matrix grain size to protect all areas of the GB from He segregation and attack.

In this work, we perform a systematic screening of crystals listed in the Materials Project database<sup>[15]</sup> and show the top candidates for the nano-phases with potentially low  $\mathcal{E}_{\text{emb}}$  and decent He absorbing capacity (10 at.% or more), which could be advantageous for soaking up and delaying He damage on fusion structural materials. The screening criteria used are 1) low neutron absorption and activation, 2) relatively large elastic moduli, and 3) atomic-scale free volume that can accommodate one or more He clusters, such as “constitutional vacancies” in some crystal lattices.<sup>[16]</sup> To that end, we first illustrate that atomic-scale free volume/pores are hallmarks of low  $\mathcal{E}_{\text{emb}}$ . Then combining experiments and calculations, we demonstrate that  $\mathcal{E}_{\text{emb}}$  is, in turn, a good ab initio predictor for our He diversion strategy in order to avoid He damage. We study a two-phase alloy consisting of TiAl ( $\gamma$ ) and  $\text{Ti}_3\text{Al}$  ( $\alpha_2$ ) nanolamellas. Density functional theory (DFT) calculations show that the  $\alpha_2$  phase has significantly lower  $\mathcal{E}_{\text{emb}}$  than the  $\gamma$  phase. Experimental He ion implantation and post-mortem TEM characterizations then show that indeed only the  $\alpha_2$  phase is significantly damaged with He bubbles, while the adjacent  $\gamma$  phases appear very much “immune” from damage. This experimental validation sets the theoretical basis for our nano-phase selection based on ab-initio computed  $\mathcal{E}_{\text{emb}}$ .

There are also important auxiliary considerations in addition to the low  $\mathcal{E}_{\text{emb}}$  and decent He absorbing capacity of the nano-phases. First, the constituent atoms of the nano-phases must be “neutron-friendly”. That is, they should not cause too much excess neutron absorption/activation in order to not complicate the neutronics of the reactor or waste disposal, or lose the He-binding effect over time. Second, the nano-phases need to be mechanically strong in tension and shear to be able to sustain significant load locally. That is, they need to still serve as the strengthening phase for creep resistance.<sup>[5,12,13]</sup> This is especially true if  $\mathcal{E}_{\text{emb}}$  (2nd phase)  $<$   $\mathcal{E}_{\text{emb}}$  (PB) and thus the PB does not debond first. Third, the fusion reactor vessel will be operating at temperatures up to 800 °C, and thus the nano-phases need to be thermally and chemically stable in contact with the matrix phase and be coarsening-resistant. Thus the solubility and diffusivity of some of the second phase’s constituent elements in the matrix phase should be very low, like O, N, etc., in the same way as ODS. Finally, in order to achieve uniform dispersion without aggregation during the processing of such structural nanocomposite, the nano-phases also need to have a low enough wetting angle with the metal matrix. Herein, we will demonstrate the down-selection of He-absorbing nano-phases, taking into account the melting

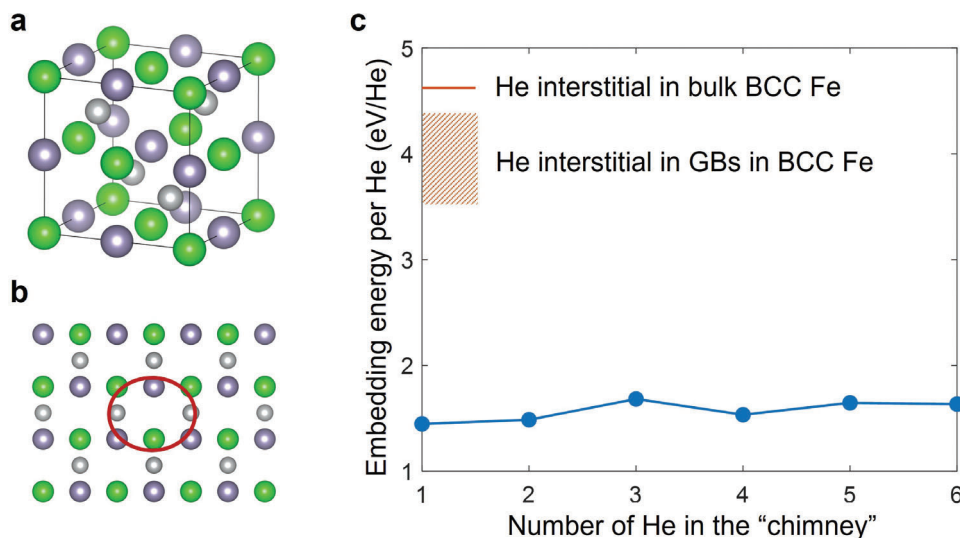


**Figure 1.** Presence of atomic-scale free volume and He embedding energy. a) Atomic structure of ZrNiSn Half-Heusler compound with constituent vacancies. b) The “free-volume chimney” in ZrNiSn along [110] direction. c)  $\mathcal{E}_{\text{emb}}$  of He atom in ZrNiSn (blue curve with dots), versus  $\mathcal{E}_{\text{emb}}$  of He interstitial in various sites in BCC Fe.  $\mathcal{E}_{\text{emb}}$  of He interstitial in GBs in BCC Fe depends on the local environment (distance from the GB, structure of the GB, etc.), and thus has a distribution, represented by the thick bar.

temperature ( $T_M$ ), the thermodynamic compatibility, and the wetting angle of the nano-phases with Fe matrix as an example.

## 2. Results

### 2.1. He-Embedding Energy in Lattice Interior and GB of Fe, Half-Heusler Phases, and Others

Before doing the high-throughput computational screening, one needs to define and validate numerical metrics of high He absorbing capability. As we will elaborate on later, low He embedding energy  $\mathcal{E}_{\text{emb}}$  (unit eV/He) can be a figure of merit. However, it is computationally demanding to do high-throughput calculations on embedding energies, which require relatively expensive supercell calculations. Here, we propose that the atomic-scale free volume can be an indicator of low embedding energy, and thus can serve as an “easy-to-compute” metric of good He-absorbing nano-phases. In the following, we will show that this assumption is verified by ab initio calculations. Since we will study He formation energy in various geometries in the following, we adopt the general term “embedding” energy rather than “interstitial formation” energy. The embedding energy is defined as

$$E_{\text{emb}}(m) \equiv E_{\text{He}_m}^{\text{tot}} - E_{\text{He}_0}^{\text{tot}} - mE_{\text{He}}, \mathcal{E}_{\text{emb}}(m) \equiv E_{\text{emb}}/m \quad (1)$$

where  $m$  is the number of He atoms,  $E_{\text{He}_m}^{\text{tot}}$  is the total energy of the system with  $m$  He atoms,  $E_{\text{He}_0}^{\text{tot}}$  is the total energy of the system without He atoms (with other atoms the same), while  $E_{\text{He}}$  is the energy of a single isolated He atom, which is 89 meV in our supercell calculation setup.

Previously, Erhart et al.<sup>[17]</sup> comprehensively investigated He interstitial formation and migration energies in various oxides, including  $\text{Al}_2\text{O}_3$ ,  $\text{TiO}_2$ ,  $\text{Y}_2\text{O}_3$ ,  $(\text{Mg}, \text{Ca}, \text{Sr}, \text{Ba})\text{O}$ ,  $\text{Y}_x\text{Al}_y\text{O}_z$ , via DFT

calculations. They found that the solubility of He in oxides scales with the free volume at the interstitial site and is virtually independent of the oxide’s chemical composition. Similar features are found in body-centered cubic (BCC) Fe as well. In Ref. [18],  $\mathcal{E}_{\text{emb}}$  for the octahedral and tetrahedral interstitial sites of BCC Fe are reported to be 4.60 and 4.37 eV/He, respectively, based on DFT calculations.<sup>[18]</sup> On the other hand, when He is associated with a Fe vacancy, which provides a larger free volume, the embedding energy  $\mathcal{E}_{\text{emb}}$  would decrease to  $\approx 4$  eV/He. Moreover, when He atoms reside in the GBs of BCC Fe, which have greater free volume,  $\mathcal{E}_{\text{emb}}$  is found to be even lower by  $\approx 1$  eV/He, providing a strong incentive for GB segregation (Figure 1c) and subsequent debonding damage, though the exact value depends on the angle and sigma value of the boundaries.<sup>[18]</sup> These results suggest that  $\mathcal{E}_{\text{emb}}$  is sensitive to the local atomic geometry, and particularly,  $\mathcal{E}_{\text{emb}}$  would be lower when the local free volume is large. This point is further corroborated by Half-Heusler (HH) phase ZrNiSn. The atomic structure of the HH phase features an extended “free volume chimney” infinitely long in a perfect crystal (Figure 1a,b). Indeed, our DFT calculations indicate that  $\mathcal{E}_{\text{emb}}$  is on the order of just 1.5 eV/He in ZrNiSn, and  $\mathcal{E}_{\text{emb}}$  per He does not increase much when multiple He atoms are put in the free-volume chimney (Figure 1c) of this crystal. This corroborates that the key to reducing  $\mathcal{E}_{\text{emb}}$  is to provide a spacious room for He atoms. While the HH phases serve as an illustration of low  $\mathcal{E}_{\text{emb}}$  and decent He absorbing capacity, the ZrNiSn compound itself is not very neutron-friendly, as Ni and Sn will have high long-term activity after exposure to fast neutrons, thus presenting a nuclear waste problem. Later, we will systematically show that the atomic-scale free volume is a good indicator of low  $\mathcal{E}_{\text{emb}}$  with first-principle calculations.

Below, combining experiments and DFT calculations, we show that the raw magnitude of  $\mathcal{E}_{\text{emb}}$  is the key feature for the strategy of He diversion and screening, and offers protection of certain phases even when the overall He injection exceeds  $10^4$  appm,

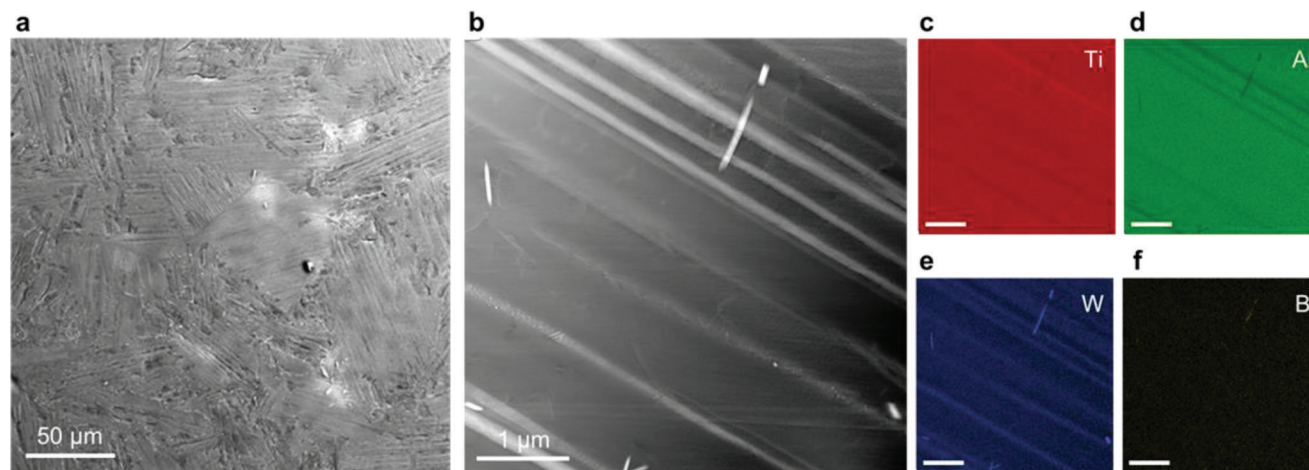


**Figure 2.** Microstructural characterization of as-fabricated Ti-48Al-2W-0.08B (at.%) alloy with  $\gamma$  (TiAl) and  $\alpha_2$  (Ti<sub>3</sub>Al) nano-lamellae. a) SEM micrograph showing equiaxed grains with interior nano-lamellar structures. b) STEM micrograph showing the two phases with  $\gamma$  phases in dark contrast and  $\alpha_2$  phase in bright contrast. c–f) EDS mapping of the major chemical composition of Ti and Al, and minor elements of W and B. Scale bars in (c–f), 1  $\mu\text{m}$ .

way more than the level typically required for a civilian fusion reactor. Subsequently, we propose that atomic-scale free volume, which indicates low  $\mathcal{E}_{\text{emb}}$ , would be a good predictor of strong He absorbing capability. Based on this rationale, we perform large-scale computational screening for potential He-absorbing nano-phases, considering also the processability, load-bearing ability, and neutronics aspects of fusion reactors.

## 2.2. Helium Diversion and Screening, Damage Avoidance in Two-Phase Ti–Al Alloy

Figure 2 shows the characterization of the as-fabricated Ti-48Al-2W-0.08B (at.%) alloy with a nano-lamellar heterophase structure using scanning electron microscopy (SEM) and scanning transmission electron microscopy (STEM). Equiaxed grains with interior nano-lamellar structures were clearly identified in the SEM micrograph (Figure 2a). The two-phase components ( $\gamma$  and  $\alpha_2$ ) in the grain interiors were distinguished in the STEM micrograph with the  $\gamma$  phase in the dark contrast and  $\alpha_2$  in the bright contrast, as shown in Figure 1b. Three types of interfaces ( $\gamma/\gamma$ ,  $\gamma/\alpha_2$ , and  $\alpha_2/\alpha_2$ ) were observed in the as-fabricated alloy. The chemistry analysis with electron dispersive spectroscopy (EDS) mapping suggests that minor element tungsten (W), which was added to improve mechanical properties, preferentially segregates to the  $\alpha_2$  phase, while depletes in the  $\gamma$  phase; the segregation of W did not change the crystal structure of the  $\alpha_2$  phase (Figure S1, Supporting Information).

To assess the He absorption behaviors of the two phases ( $\gamma$  and  $\alpha_2$ ) in the Ti-48Al-2W-0.08B alloy, He ion implantations were performed at 750 °C. Figure 3 reveals the microstructural evolution of the nano-lamellar  $\gamma/\alpha_2$  under He irradiation—the Stopping and Range of Ions in Matter (SRIM) calculation results are provided in Figure S2 (Supporting Information). The  $\gamma$  and  $\alpha_2$  phases show a significant difference in He gas bubble formation. A high density of He gas bubbles ( $\approx 2 \times 10^{22} \text{ m}^{-3}$ ) formed in the  $\alpha_2$  phase, while the density of He gas bubbles in the  $\gamma$  phase is lower by a factor of  $\approx 7$ , and there was no noticeable

interfacial segregation of He bubbles. The He bubbles in both phases are faceted as shown in Figure 3a,b. No clear evidence of a bubble-denuded zone was observed near the interfaces. The chemical mapping in Figure 3c–f suggests that no clear chemical segregation occurs near the bubbles or the interfaces. In the  $\alpha_2$  phase, some features in white contrast form in the vicinity of faceted He gas bubbles. The high-resolution TEM micrograph implies that irradiation-induced planar faults form associated with the formation of He gas bubbles (Figure S3, Supporting Information).

## 2.3. Effect of He Embedding and Migration Energies on the Distribution of He Bubbles

The experimental results described above imply that the  $\alpha_2$  phase may have a higher He absorbing capability. To understand this phenomenon, DFT calculations were performed. We first investigated the He migration energies,  $Q_{\text{m}}$ . The minimum  $Q_{\text{m}}$  is found to be 0.31 eV for the  $\alpha_2$  phase when the He atoms migrate along the crystallographic  $c$ -axis. For the  $\gamma$  phase, the minimum  $Q_{\text{m}}$  is 0.43 eV when He atoms migrate along the  $a$ -axis (or equivalently  $b$ -axis). At the experimental ion-radiation temperature of 750 °C ( $T = 1023 \text{ K}$ ),  $Q_{\text{m}} = 0.43 \text{ eV}$  will lead to He interstitial lattice diffusivity as high as  $D_{\text{He}} = 10^{-10} \text{ m}^2 \text{ s}^{-1}$ . Since the characteristic diffusion distance scales as  $(2D_{\text{He}}t)^{1/2}$ , this means  $>10 \mu\text{m}$  diffusion distance if just holding for  $t = 1 \text{ s}$ , which is much greater than the  $\gamma$ - $\alpha_2$  lamella spacing. These results indicate that “distance is no object” and He atoms anywhere can easily migrate to the nearest lower-embedding energy phase ( $\alpha_2$ ), explaining the higher density of He gas bubbles in the  $\alpha_2$  phase observed in the experiment, while the  $\gamma$  phase shows much less He damage. Together with the calculations on  $\mathcal{E}_{\text{emb}}$  below, this proves that the lower- $\mathcal{E}_{\text{emb}}$  region can indeed shield/screen the higher- $\mathcal{E}_{\text{emb}}$  region largely from He damage, even with  $\Delta\mathcal{E}_{\text{emb}}$  as small as 0.5 eV/He (see DFT calculation below). And if we are interested in protecting ferritic/martensitic steels, since  $\mathcal{E}_{\text{emb}}$  in BCC Fe’s grain boundaries is on the order of 4 eV/He (see Figure 1c), all we need to do

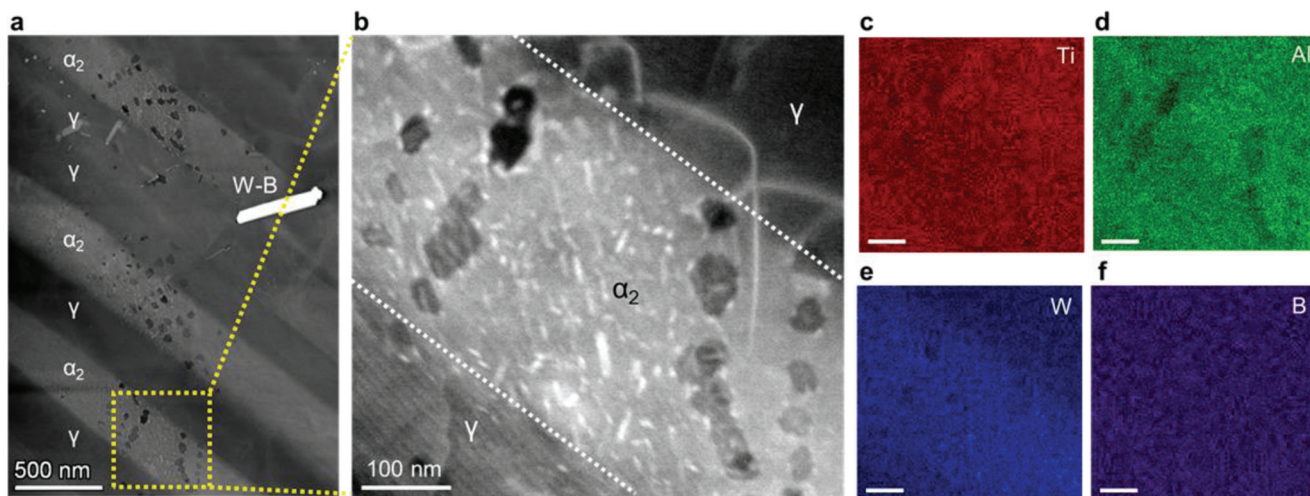


**Figure 3.** Characterization of He-irradiated Ti-48Al-2W-0.08B alloy at 750 °C with 10000 appm He. a) STEM micrograph showing the peak damage region of Ti-48Al-2W-0.08B alloy. b) Enlarged view of the boxed region in (a). A high density of He gas bubbles ( $\approx 2 \times 10^{22} \text{ m}^{-3}$ ) form in the  $\alpha_2$  phase, while a much lower density of He gas bubbles forms in the  $\gamma$  phase. (c–f) EDS map showing no evidence of chemical segregation in the vicinity of He bubbles and interfaces. Scale bars in (c–f), 100 nm.

for protecting such steels is to seek easy-to-disperse He-absorbing nano-phases with  $\mathcal{E}_{\text{emb}} < 3 \text{ eV/He}$ .

Next, we illustrate that the He embedding energy  $\mathcal{E}_{\text{emb}}$  strongly influences the He absorbing capability. We first considered pristine titanium aluminides without any defects. Single He atom was put in several inequivalent locations in the titanium aluminides and then the atomic structure was relaxed until the forces on each atom are lower than  $5 \times 10^{-3} \text{ eV/\AA}$ . The minimum embedding energies are found to be 2.89 and 3.36 eV/He for the  $\alpha_2$  and  $\gamma$  phases, respectively. Thus,  $\mathcal{E}_{\text{emb}}$  of the  $\alpha_2$  phase is lower than that of the  $\gamma$  phase by 0.47 eV/He. Also, defects such as vacancies are inevitable in a lot of engineering materials. Hence we also investigated  $\mathcal{E}_{\text{emb}}$  values for Ti and Al lattice vacancies in titanium aluminides, which provide a relatively spacious room for the He atoms and can potentially host them with lower energy costs. When a single He atom resides in their vacancy sites,  $\mathcal{E}_{\text{emb}}$  is found to be  $\approx 1.5 \text{ eV/He}$  for both  $\alpha_2$  and  $\gamma$  phase titanium aluminides, which is only half of the values for pristine  $\alpha_2$  and  $\gamma$  phases without vacancies (Figure 4).

The He absorbing capability may be further enhanced if a single vacancy site can trap multiple He atoms. To test this speculation, we put more He atoms in a single vacancy site and studied how the embedding energy per He atom  $\mathcal{E}_{\text{emb}} \equiv E_{\text{emb}}/N_{\text{He}}$  varies with  $N_{\text{He}}$ . The results are shown in Figure 4a,b. For the  $\gamma$  phase (Figure 4b), one can see that  $\mathcal{E}_{\text{emb}}$  increases from  $\approx 1.5$  to  $\approx 3 \text{ eV/He}$  when  $N_{\text{He}}$  increases from one to four. Then  $\mathcal{E}_{\text{emb}}$  stops increasing when more He atoms are put into the vacancy site in the initial structure. This is because some He atoms migrate to other sites spontaneously after the atomic structure relaxation in DFT calculations, indicating that a maximum of four He atoms may reside in a single vacancy site in  $\gamma$  phase TiAl. In contrast, the  $\mathcal{E}_{\text{emb}} \cdot N_{\text{He}}$  curve shows more interesting features for the  $\alpha_2$  phase  $\text{Ti}_3\text{Al}$  (Figure 4a)— $\mathcal{E}_{\text{emb}}$  drops significantly for certain  $N_{\text{He}}$ , showing “magic numbers” features well known in cluster physics. For example, in the case of the Al vacancy,  $\mathcal{E}_{\text{emb}}$  is below 1.5 eV/He when  $N_{\text{He}} = 5$ , while for  $N_{\text{He}} = 4$  and 6,  $\mathcal{E}_{\text{emb}}$  is

higher than 2.3 eV/He. We examined the atomic structure with  $N_{\text{He}} = 5$  and found that a triangular bipyramid He complex is formed. Such complexes are bound not by chemical bonds, but by van der Waals attractions, and have dissociation energies much weaker than those of chemically bonded species.<sup>[19]</sup> Yet, the high-symmetry van der Waals complexes can reduce the total energy, leading to a lower  $\mathcal{E}_{\text{emb}}$ . Similarly, in the case of  $\alpha_2$  phase  $\text{Ti}_3\text{Al}$  with Ti vacancy, a tetrahedral He complex forms when  $N_{\text{He}} = 4$ , which again reduces  $\mathcal{E}_{\text{emb}}$ . This may explain the high He absorbing capability of the  $\alpha_2$  phase  $\text{Ti}_3\text{Al}$  observed in experiments, as compared with the  $\gamma$  phase TiAl where the optimal  $N_{\text{He}}$  is tightly one even with Ti- or Al-site vacancies. These results also imply that He clusters in some phases can become metastable when the number of He atoms reaches certain values (e.g., 5); such metastability can in turn promote the formation of new clusters rather than the growth of existing clusters. The analysis above can be further verified by the trend of the marginal energy cost to add each He in the vacancy site [i.e.,  $E_{\text{emb}}(N_{\text{He}}) - E_{\text{emb}}(N_{\text{He}} - 1)$ ]. One can see that the energy cost can be very small, and even turns negative when the additional He atom leads to the formation of the high-symmetry He van der Waals complexes (Figure 4c).

#### 2.4. High-Throughput Screening of He-Absorbing Nano-Phases

Combining insights from experiments and computations, one can see that atomic-scale free volume, either with or without constitutional vacancies,<sup>[16]</sup> can significantly decrease He embedding energy  $\mathcal{E}_{\text{emb}}$ . Given the matrix phase typically have either BCC or face-centered cubic (FCC) structures with low free volume (see the left portion of Figure 5a before the graph break), we expect that secondary phases are necessary to introduce such atomic-scale free volume (see the right portion of Figure 5a after the graph break). Moreover, to prevent adverse effects on the fracture toughness, the size of these secondary phases  $D$  is desirable to be small (preferably  $D$  below  $\approx 20 \text{ nm}$ <sup>[20,21]</sup>) as the oxide

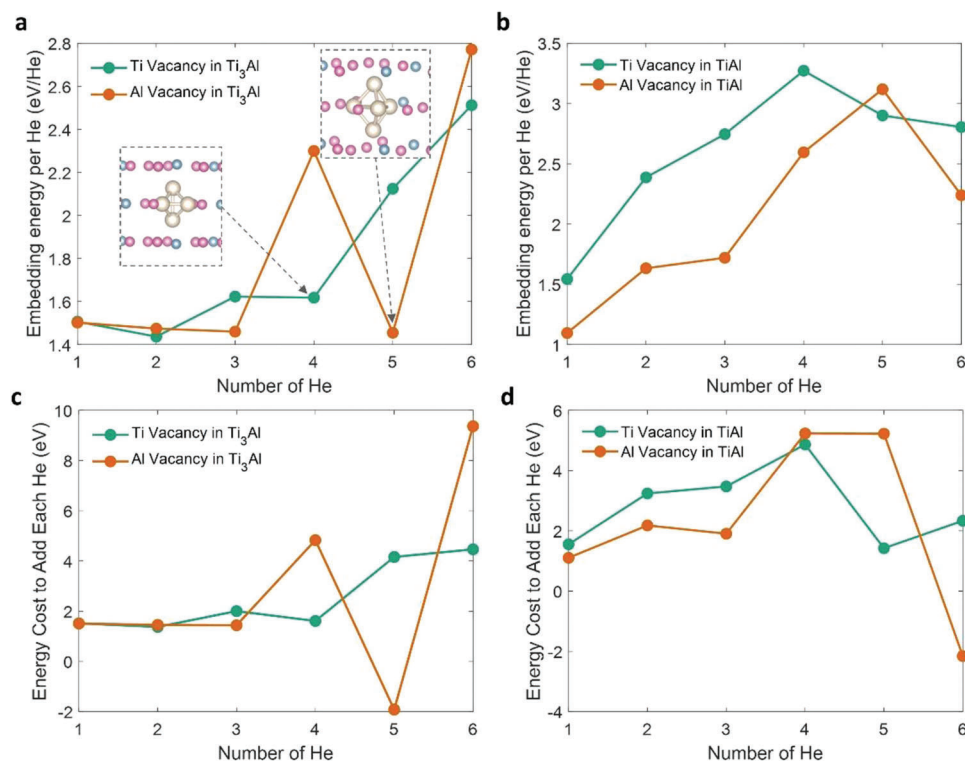


**Figure 4.** a, b) Embedding energy per He atom  $\mathcal{E}_{\text{emb}}$  as a function of the number of He atoms  $N_{\text{He}}$  that are put into a single vacancy site for a)  $\alpha_2$  phase and b)  $\gamma$  phase titanium aluminides. The green and red curves are for Ti and Al vacancies, respectively. Insets of (a) show the relaxed local structures of the He complexes for  $N_{\text{He}} = 4$  in Ti vacancy and  $N_{\text{He}} = 5$  in Al vacancy in the  $\alpha_2$  phase, respectively. Purple: Ti; Blue: Al; Light beige: He. c, d) The marginal energy cost to add each He [ $E_{\text{emb}}(N_{\text{He}}) - E_{\text{emb}}(N_{\text{He}} - 1)$ ]. In (d), the marginal energy cost appears low when the number of He is  $>4$ , because the He escapes the vacancy site during the relaxation in DFT calculations.

nanodispersions in ODS alloys. This size level would relieve the requirement for long-range He migration as well. Here we carried out high-throughput screenings for all compounds in the Materials Project database<sup>[15]</sup> with Inorganic Crystal Structure Database (ICSD) numbers.<sup>[22]</sup> In the following, we will discuss the screening process in sequential order.

#### 2.4.1. Neutron Absorption Cross-Section

To ensure that He-absorbing nano-phases are neutron friendly, we consider only compounds consisting of elements with a thermal neutron absorption cross-section below 1 barn, and a residual activity smaller than  $10^5$  MBq  $\text{kg}^{-1}$  10 years after 2 full-power years of operation under DEMOnstration Power Plant (fusion DEMO) first wall and vacuum vessel radiation fields (see Figure 9 of Ref. [23]). Neutrons engendered as a product of burning plasma fusion need to reach a blanket, where they react with lithium-6 to produce further tritium fuel for fusion reactions and heat up the coolant to drive a steam turbine and produce electricity.<sup>[11]</sup> Therefore, the first wall and vacuum vessel, which are present in between neutron-yielding plasma and the blanket, should have small neutron cross-sections to allow the neutrons to stream through without significant absorption. This neutron cross-section criterion leaves the following elements as adoptable constituents for He-absorbing nano-phases: aluminum (neutron absorption cross-section  $\sigma_a = 0.232$  barn), beryllium (0.0092

barn), bismuth (0.034 barn), calcium (0.43 barn), carbon (0.0035 barn), fluorine (0.0096 barn), hydrogen (0.3326 barn), lead (0.171 barn), magnesium (0.063 barn), oxygen (0.00019 barn), phosphorous (0.172 barn), rubidium (0.38 barn), silicon (0.171 barn), sodium (0.53 barn), sulfur (0.53 barn), and zirconium (0.184 barn). Helium, neon, polonium, cerium, and platinum also meet this criterion but got excluded, being either inert, radioactive, or expensive. Compounds consisting of other elements were excluded in this first stage of the screening process.

#### 2.4.2. Neutron Activity

Another important factor in designing fusion structural materials is neutron activity. Following the exposure to neutrons inside a fusion reactor, a certain amount of time is required for the material to decay to low-level waste limits ( $< 4$  MBq  $\text{kg}^{-1}$  for alpha radiation and  $< 12$  MBq  $\text{kg}^{-1}$  for combined gamma and beta radiation).<sup>[24]</sup> The elements with high neutron activation over long time horizons are thus undesirable from the nuclear-waste-disposal point of view. Here we used  $10^2$  MBq  $\text{kg}^{-1}$  as an upper limit since the matrix material is likely to be either Fe or Ni, of which activities are  $\approx 10^2$  MBq  $\text{kg}^{-1}$  10 years after shutdown, assuming their use as a vacuum vessel component in a DEMO reactor for 2 years of full operation.<sup>[24]</sup> This criterion then excludes cesium, cobalt, europium, lithium, samarium, and tellurium; in fact, these elements were already excluded

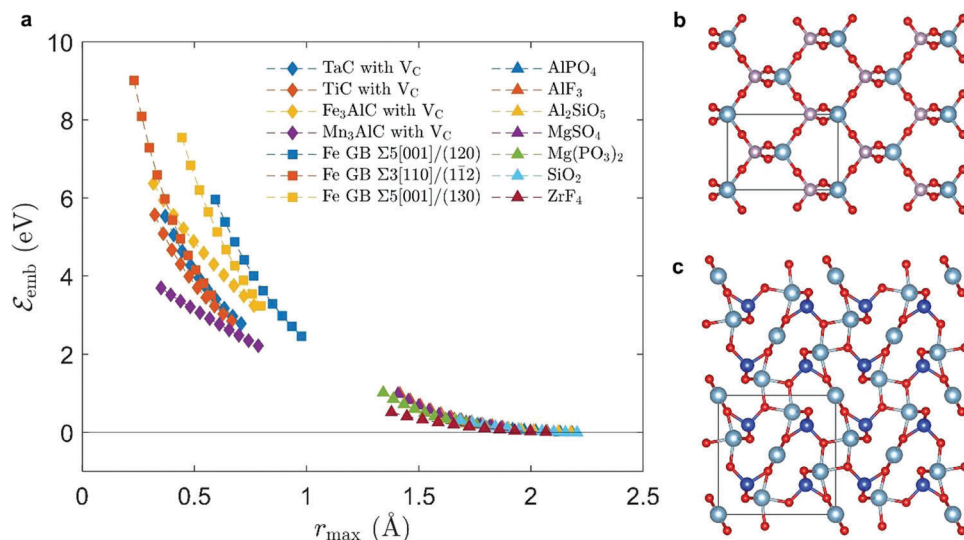


**Figure 5.** a)  $\mathcal{E}_{\text{emb}}$  as a function of  $r_{\text{max}}$  for candidate materials in Table 1, carbides with carbon vacancy, and GB in BCC Fe. b,c) Crystal structures of b)  $\text{AlPO}_4$  and c)  $\text{Al}_2\text{O}_3 \cdot \text{SiO}_2$ , which were identified to be candidate materials for He-absorbing nano-phases with large atomic-scale free volume. The black box in (b, c) indicates the unit cell.

by absorption cross-section consideration, and thus, there will be no difference in the list of usable elements. One should note that long-term activation should be considered for more thorough screening, but since the amount of the He-absorbing nano-phases would be on the order of 0.5 to 2 wt.% for acceptable mechanical properties, the activation by the added He-absorbing nano-phases would no longer be a problem provided that all the constituting elements have an activity  $< \approx 10^2 \text{ MBq kg}^{-1}$ , being reduced by two orders of magnitude.

#### 2.4.3. Elastic Moduli

For the next stage of the screening process, we exclude compounds with an average bulk modulus  $B$  smaller than 50 GPa or an average shear modulus  $G$  smaller than 20 GPa to ensure that the candidate materials are mechanically strong inclusions. The nano-phases need to be capable of sustaining significant load imposed by absorbed He locally and resist dislocation cutting<sup>[13,25]</sup>—after all, the difference between a second-phase oxide in ODS and a gas-filled cavity is that tensile stress can be transmitted across the former, while a cavity has zero moduli and sheds load on the surrounding metal. We can estimate this resistance by computing the second phase's elastic moduli. To that end, we utilized the dataset of elastic constants calculated from first-principles DFT.<sup>[26]</sup> For materials not included in Ref. [26], we used the statistical learning predictions of the elastic properties, which were developed in Ref. [27]. Our results indicate that despite the atomic-scale free volume, many compounds still have large moduli and potentially good mechanical robustness.

#### 2.4.4. Free Volume

Finally, we considered the capability to absorb He. As discussed before, low He embedding energy is closely related to strong

He absorbing capability. However, high-throughput calculations of He embedding energy, which requires large supercells, can be computationally demanding. Hence, we resort to “easy-to-compute” metric. Based on previous analyses, we found that the size of the free volume to accommodate He atoms can be a tell-tale signature that indicates low He embedding energy and large He absorbing capability. In this regard, we selected compounds with intermediate pore volumes in their crystal structures, which can potentially host He atoms with small embedding energies. We quantified the size of the free volume by the radius ( $r_{\text{max}}$ ) of the largest sphere that can be fitted in the crystal structure, without any atoms inside the sphere. Crystal structures used for the quantification are perfect lattices without any defects. One should also note that each atom in the host material is represented by a sphere whose radius is the covalent radius of the atoms instead of the ionic radius due to difficulties in taking into account its dependence on coordination numbers; we discuss later how well the  $r_{\text{max}}$  obtained using covalent radii correlates with the  $\mathcal{E}_{\text{emb}}$ . We then calculated  $r_{\text{max}}$  for all compounds that survived the previous two screening processes and kept only compounds with  $r_{\text{max}} > 1.5 \text{ \AA}$ . The  $r_{\text{max}}$  required to fit a He tetrahedron is  $\approx 1.7 \text{ \AA}$  when calculated using the van der Waals radius of He; however, since some atomic-scale free volume can be elliptical, 1.5 Å is used for screening purpose. More stringent screening can be conducted by using a larger  $r_{\text{max}}$ . The full list of potentially He-absorbing nano-phases obtained through these screening processes is provided in the Table S1 (Supporting Information), along with the estimated moduli and the size of the free volume.

#### 2.4.5. Melting Temperature, Phase Compatibility, and Wettability

When it comes to the processing and fabrication of a nanocomposite (by sintering, casting, or 3D printing<sup>[28]</sup>), the melting temperature, phase compatibility with the matrix, and wettability by the matrix material also become important for the selection

**Table 1.** List of Possible He-Absorbing Nano-Phases and their Compatibility with an Exemplary Matrix, Fe.

Chemical formula	Material project ID	Avg. bulk modulus [GPa]	Avg. shear modulus [GPa]	$r_{\max}$ [Å]	Wetting angle [deg.] <sup>a)</sup>	Melting point [°C]	Phases at 800 °C for Fe with 1 wt.% of He-absorbing nano-phase
Al <sub>2</sub> SiO <sub>5</sub>	mp-4753	155.8	97.5	1.90	81.8	1840	Fe + mullite [xAl <sub>2</sub> O <sub>3</sub> ·ySiO <sub>2</sub> ] + quartz [Si-O] + spinel [Fe-Al-O]
AlPO <sub>4</sub>	mp-7848	84.6	48.2	1.92	90.2	1800	Fe + halite [Fe-Al-O]
SiO <sub>2</sub>	mp-546794	93.8	57.5	1.93	95.1	1710	Fe + quartz [SiO <sub>2</sub> ]
AlF <sub>3</sub>	mp-468	116.1	53.0	1.64	89.1	1291	Fe + AlF <sub>3</sub> <sup>b)</sup>
Mg(PO <sub>3</sub> ) <sub>2</sub>	mp-18620	113.5	60.8	1.57	96.5	1160	Fe + halite [Fe-Mg-O]
MgSO <sub>4</sub>	mp-4967	106.8	51.5	1.64	97.8	1124	Fe + halite [Fe-Mg-O] + pyrrhotite (Fe-S)
ZrF <sub>4</sub>	mp-561384	133.4	54.7	1.73	97.2	910	Fe + ZrF <sub>4</sub> <sup>b)</sup>

<sup>a)</sup> Wettability by molten Fe at 1600 °C; <sup>b)</sup> Equilibrium phases predicted by Materials Project database.<sup>[15]</sup>

of the nano-phase. To be more specific, the fusion reactor vessel will be operating at temperatures up to 800 °C, and during manufacturing, the transient temperature could be even greater depending on the fabrication techniques used. The nano-phase should thus be designed not to melt or dissolve into the metal matrix at the operating/manufacturing temperatures. Such phase compatibility can be checked by the CALPHAD of PHase Diagrams (CALPHAD) method.<sup>[29]</sup> Moreover, it is important to disperse nano-phases uniformly throughout the matrix since aggregation can make their interface with the matrix have a longer end-to-end distance, which is detrimental from the stress amplification factor considerations (recall that oblate opening gives stress amplification factor  $\rightarrow\infty$ , while spherical and prolate do not when the end-to-end distances  $\rightarrow\infty$ ). To enable uniform dispersion, the nano-phases need to have a low enough wetting angle with the metal matrix. The wettability can be examined using the machine-learning equilibrium wetting angle ( $\theta$ ) prediction<sup>[30]</sup> method that we recently developed, which can predict arbitrary ceramic-metal wetting angles. It should also be noted that diffusion may be available at such operating temperature, and hence, the nano-phases could coarsen by the Gibbs-Thompson effect.<sup>[31]</sup> Fortunately, for many metal matrices, due to the low solubility of oxygen, nitrogen, etc., the nano-phases are relatively stable (e.g., ODS steels) and coarsening-resistant.

To demonstrate initial down-selection of He-absorbing nano-phases with the above practical requirements, we took Fe as an exemplary matrix material. Since a method of predicting the melting temperature is available only for a limited range of ceramic materials,<sup>[32]</sup> here we screened the candidate materials first using wetting angle values. Ideally, wetting angles should better be smaller than 90°, but since only a handful of compounds meet all the aforementioned requirements simultaneously, we relieved the wetting angle limit to 100°. We then considered melting temperatures and excluded compounds with a melting temperature lower than 800 °C and examined the remaining compounds' phase compatibility with Fe via CALPHAD calculations using the Thermo-Calc software with TCFE8 database. The weight fraction of the He-absorbing phases was set to be 1 wt.%. For compounds with elements that are not included in the TCFE8 database, the phase compatibility was examined using the Materials Project database.<sup>[15]</sup>

**Table 1** shows the resulting list of He-absorbing nano-phases for Fe. SiO<sub>2</sub> was the only compound that survived the down-selection processes among those that can be examined via CALPHAD calculations. Based on thermodynamic calculation (Figure S4, Supporting Information), the phase is predicted to be quartz. The crystal structure of the SiO<sub>2</sub> that would appear at 800 °C is expected to be either P6<sub>2</sub>22 or P6<sub>4</sub>22 (mp-6922 or mp-10851 SiO<sub>2</sub>), which is called  $\beta$ -quartz<sup>[33]</sup> and is different from that of the mp-546794 SiO<sub>2</sub> in Table 1, I42d. The  $r_{\max}$ , the bulk modulus, and the shear modulus of the  $\beta$ -quartz are estimated to be 1.40 Å, 109.8, and 67.8 GPa, respectively. The  $r_{\max}$  is smaller than the criterion we used for screening, but He embedding energy is found to be very low ( $\approx 0.1$  eV), as compared with that of the GBs of BCC Fe in Figure 1c. Therefore, we expect that SiO<sub>2</sub> should be an attractive He-absorbing nano-phase for Fe-based alloys. Such composites would better be prepared by low-temperature manufacturing techniques that do not involve Fe melt since SiO<sub>2</sub> is predicted to melt at  $\approx 1450$  °C when in contact with Fe, which is lower than the melting point of Fe (Figure S4, Supporting Information).

On the other hand, AlPO<sub>4</sub>, Mg(PO<sub>3</sub>)<sub>2</sub>, and MgSO<sub>4</sub> turned out to react with Fe and form other phases with phosphorus and sulfur elements being dissolved into the Fe matrix. Al<sub>2</sub>SiO<sub>5</sub> would also react to form quartz and spinel phases, but it is still a viable option now that there remain mullite and quartz, which have large atomic-scale free volume. Since fluorine is not included in the TCFE8 database, no detailed phase information is available for AlF<sub>3</sub>, and ZrF<sub>4</sub>; however, all these compounds are predicted to be thermodynamically stable when in contact with Fe at 0 K based on Materials Project database,<sup>[15]</sup> having direct tie-lines with BCC Fe (Figure S5, Supporting Information). It should be noted that the equilibrium phase and the corresponding moduli and  $r_{\max}$  value could differ from those listed in Table 1 and that actual melting can take place at lower temperatures as the materials will be in contact with Fe.

## 2.5. Feasibility of the Identified Candidate Materials

To further verify that large  $r_{\max}$  is an appropriate indicator of low  $\mathcal{E}_{\text{emb}}$ , we artificially strain the materials in Table 1, so that  $r_{\max}$



can be modified continuously, then  $\mathcal{E}_{\text{emb}}$  as a function of  $r_{\text{max}}$  is calculated using DFT calculations. The results are shown in Figure 5a. One can see that the  $r_{\text{max}}$  versus  $\mathcal{E}_{\text{emb}}$  relationship almost collapses onto the same curve for candidates listed in Table 1. All of them showed  $\mathcal{E}_{\text{emb}}$  far below that of the GBs of BCC iron ( $\geq 3$  eV/He) and even smaller than that of most Y-M-O oxides (where M = Ti, Zr, Hf, Al; 0.59–3.14 eV/He<sup>[34]</sup>), which have been investigated extensively for the development of irradiation-resistant alloys. The atomic structures of two exemplary compounds  $\text{AlPO}_4$  and  $\text{Al}_2\text{O}_3 \cdot \text{SiO}_2$  are illustrated in Figure 5b,c. The sizes of the atomic-scale free volume are 1.9 Å for  $\text{AlPO}_4$  and 1.7 Å for  $\text{Al}_2\text{O}_3 \cdot \text{SiO}_2$ . Using DFT calculations, the He embedding energies  $\mathcal{E}_{\text{emb}}$  are found to be 0.08 and 0.10 eV/He for  $\text{AlPO}_4$  and  $\text{Al}_2\text{O}_3 \cdot \text{SiO}_2$ , respectively, which are exceptionally low and far below that of the GBs of BCC iron, where the size of the free volume is found to be below 1 Å (the exact size is dependent on the angle and sigma value of the boundaries). This, combined with the experimental demonstration in Figure 3, gives us high confidence that these nano-phases can soak up the He and protect the GB if they are distributed uniformly and close enough to the GB.

The possibility that He atoms and vacancies (V) self-aggregate in the nano-phase to form He bubbles needs to be assessed. Consider vacancy–helium complex  $V_n\text{He}_m$ . We distinguish between the situation of  $n = 0, m \geq 1$  which covers the majority of the computational screening we have done where one relies on natural free volume in the crystal without any vacancy, with  $n \geq 1, m \geq 1$  “He bubbles”. For fixed  $n$ , the existence of an optimal  $m$  that is *very small* could be advantageous in retarding coarsening. Figure 4c,d show the marginal energy cost of  $V_n\text{He}_{m-1} \rightarrow V_n\text{He}_m$ , i.e.,  $\frac{\partial E}{\partial m}|_n \equiv \mu_{\text{He}}$ , the chemical potential of He. We see that  $\mu_{\text{He}}$  is often minimized at  $N_{\text{He}} = m = 1$ . Then, the growth/coarsening of existing clusters in  $m$  would be less favorable compared to the formation of new clusters since He complexes with larger  $N_{\text{He}}$  become metastable. Also, the coalescence of multiple clusters  $V_n\text{He}_m, V_n\text{He}_m$ , inside the nano-phase may be kinetically facilitated by the imbalance in the hydrostatic stress exerted by the different He clusters to break bonds in between. The suppression of the growth/coarsening due to a small optimal  $m$  would limit the hydrostatic stress and its imbalance, respectively. Hence, the evolution of He bubbles to the critical size would take a longer time. This may be the case in the very early stage of irradiation, where dpa is small ( $< 1$ ). However, under irradiation at high temperature, the size of the atomic-scale free volume may grow via vacancy diffusion accelerated by radiation knock-out, thermal activation, etc. without requiring deviatoric stress, facilitating the evolution of He bubbles. That said, if the evolved He bubbles remain inside a nano-phase like in Figure 3b being “0D” openings, they are still less damaging as compared to He segregating at GBs, which are “2D.” The composite with such He-absorbing nano-phases would thus be more tolerant against embrittlement even when He bubbles eventually evolve in size.

There also remains the question of whether scalable fabrication of metal matrix composites with such nano-phases is achievable, which has been a long-standing hurdle in the industrialization of oxide-dispersion-strengthened alloys. In this regard, further exploration of advanced manufacturing methods is desired. For example, the formation of  $\text{SiO}_2$  nanodispersions by internal oxidation during selective laser melting was reported;<sup>[35]</sup> this finding indicates that adding inoculants that

can play a role as nucleation sites, thereby promoting the formation of nanoscale  $\text{SiO}_2$ , could enable mass production. In addition, carbides and nitrides, which are typically more dispersible as compared to oxides, could also be a good compromise in the short run. If we loosen the neutron cross-section constraint, more transition metal carbides/nitrides become available. In particular, compounds with empty substitutional sites (“constitutional vacancies”) such as interstitial carbides (e.g., TiC, VC) or  $\kappa$ -carbides (Fe, Mn)<sub>3</sub>AlC could also be useful for He shielding. Early transition metals (i.e., group IV, V, and VI elements) have relatively large atomic radii and thereby have a carbon/metal atomic radii ratio smaller than 0.59.<sup>[36]</sup> Carbides of these elements thus typically form a crystal structure where two FCC lattices are interpenetrating, which can also be viewed as an FCC array of transition metals with the carbon atoms inside the octahedral interstitial sites. These compounds often have large non-stoichiometric ranges and can introduce constitutional carbon vacancies up to  $\approx 10$  at.%. Moreover,  $\kappa$ -carbides, which have a perovskite-type crystal structure, have inherent vacant sites in their perfect lattices.<sup>[37]</sup> The He embedding energy of the vacancies in such compounds is relatively large as compared to those of the compounds identified by atomic-scale free volume screening, as shown in Figure 5a. Nonetheless, it is still comparable to or smaller than that of the GBs of BCC iron, implying that the He atoms can be partitioned to the constitutional vacancies of these compounds rather than localizing onto the GBs. When coarsening resistance is considered, interstitial nitrides or  $\kappa$ -nitrides (Fe, Mn)<sub>3</sub>AlN may also be of interest since the solubility of nitrogen in transition metals (e.g., Fe)—the primary constituent elements of the materials for structural components—is generally lower than that of carbon.

### 3. Discussions

In this paper, the effects of He embedding and migration energies in soaking up and shielding He damage were explored via He implantation experiment, post-mortem TEM characterization, and DFT calculations. The results demonstrate that the incorporation of nano-heterophases with  $\Delta\mathcal{E}_{\text{emb}}$  as small as 0.5 eV/He can guide He atoms where to reside at 750 °C. Also, calculations show that the optimal number of He atoms for a He cluster is discretized (“magic numbers” in cluster physics) and often quite small (e.g.,  $N_{\text{He}} = 1$  to 5), before the cluster would spontaneously break up. These details need to be accounted for when computing the exact He uptake capacity in designing secondary phases, some having few-percent constitutional vacancies.

Based on these findings, high-throughput screening to identify potentially compelling He-absorbing nano-phases was conducted using the following criteria: the compound should 1) consist of neutron-friendly elements with a neutron absorption cross-section and residual radioactivity smaller than 1 barn and  $10^2$  MBq kg<sup>-1</sup> ten years after 2-year service, respectively; 2) have a bulk modulus and an average shear modulus  $> 50$  and 20 GPa, respectively, to be able to be load-bearing; and 3) have atomic-scale free volume with a radius  $> 1.5$  Å. Given the requirements, we have identified certain silicates, phosphates, and  $\text{SiO}_2$ - $\text{Al}_2\text{O}_3$ -based crystals and even glasses to be of great utility for soaking up He and shielding the matrix grain boundary network. Furthermore, compounds with few percent constitutional vacancies such

as interstitial carbides/nitrides,  $\kappa$ -carbides/nitrides, and yttria-stabilized zirconia (YSZ)—8 mol.% YSZ having up to 4 at.% oxygen vacancies—may also shield GBs from He embrittlement. The nano-phases identified in this work via the materials genomics search could help fusion structural materials become capable of soaking up a few-thousand appm of He and shielding the matrix GBs from He damage—the main cause of their He embrittlement, while also providing superior high-temperature creep resistance and dpa resistance like the ODS alloys.

## 4. Experimental Section

**Materials Fabrication, Irradiation, and Characterization:** Ti-48Al-2W-0.08B (at.%) alloys were fabricated using a spark plasma sintering process.<sup>[38]</sup> A minimal amount of tungsten was added to improve mechanical properties. Two distinct microstructures were created by varying the processing conditions. Ti-48Al-2W-0.08B alloy with semi-coherent nano-lamellar  $\gamma/\alpha_2$  structures was fabricated under 50 MPa at 1375 °C. The measured temperatures were 60 °C below the actual sample temperatures due to the thermal gradient between the sample and the location where the temperatures were measured. He ion implantation was performed at 750 °C to a fluence of  $1.6 \times 10^{16} \text{ cm}^{-2}$  using He ions with the energy of 800 keV. The He concentration was calculated to be  $\approx 10000$  atomic-parts-per-million (appm) at the penetration depth of  $\approx 2.25 \mu\text{m}$  beneath the surface by the Stopping and Range of Ions in Matter (SRIM) code with Kinchin-Pease approximation<sup>[39,40]</sup> (Figure S2, Supporting Information). The microstructure of Ti-48Al-2W-0.08B alloys was characterized by LYRA 3 TESCAN SEM and FEI Titan TEM. A TEM-based EDS imaging was used to probe the chemical distribution in the as-fabricated and irradiated specimens.

**Density Functional Theory Calculations:** The Vienna ab initio simulation package (VASP)<sup>[41]</sup> was used to do the ab initio calculations based on density functional theory (DFT).<sup>[42,43]</sup> The exchange-correlation interactions were treated by generalized gradient approximation (GGA) in the form of Perdew-Burke-Ernzerhof (PBE).<sup>[44]</sup> The core and valence electrons were treated by projector augmented wave (PAW) method<sup>[45]</sup> and plane-wave basis functions, respectively. Supercells with a length  $> 10 \text{ \AA}$  along each dimension were used to calculate the He embedding energies, and the first Brillouin zone was sampled by a  $3 \times 3 \times 3 \text{ k}$ -mesh. The atomic structure was relaxed until the force on each atom was  $< 5 \times 10^{-3} \text{ eV/\AA}$ .

**Thermodynamic Calculations:** Equilibrium phases were identified using the CALculation of PHase Diagrams (CALPHAD) technique in conjunction with Thermo-Calc software. TCFe8 databases for Fe-based alloys were used. The calculations were carried out for compositions corresponding to Fe with 1 wt.% of He-absorbing nano-phases.

**High-Throughput Materials Screening:** The Python Materials Genomics (pymatgen) package was used to retrieve information (compositions, atomic structures, etc.) on all compounds in the Materials Project database,<sup>[15]</sup> and the Atomic Simulation Environment (ASE) package<sup>[46]</sup> was used to analyze the atomic structures.

## Supporting Information

Supporting Information is available from the Wiley Online Library or from the author.

## Acknowledgements

This work was supported by Eni S.p.A. through the MIT Energy Initiative. S.Y.K. gratefully acknowledges partial financial support by the Kwanjeong Scholarship. C. S. acknowledges the support by the U.S. Department of Energy, Laboratory Directed Research and Development (LDRD) program at Idaho National Laboratory, under contract No. DE-AC07-051D14517. T.V.

acknowledges the auspices of the U. S. Department of Energy by Lawrence Livermore National Laboratory under contract No. DE-AC52-07NA27344. The calculations in this work were performed in part on the Texas Advanced Computing Center (TACC) and MIT engaging cluster.

## Conflict of Interest

The authors declare no conflict of interest.

## Author Contributions

H.X. and S.Y.K. contributed equally to this work. H.X., S.Y.K., C.S., and J.L. designed the research inspired. J.-P.M. and T.V. prepared samples. D.C. carried out He ion implantation. C.S. performed transmission electron microscopy analysis. H.X. conducted density functional theory calculations. S.Y.K. conducted thermodynamic calculations. H.X. and S.Y.K. analyzed the results and worked on high-throughput screening. H.X., S.Y.K., C.S., and J.L. wrote the paper. All authors contributed to the discussion of the results and commented on the manuscript.

## Data Availability Statement

The data that support the findings of this study are available from the corresponding author upon reasonable request.

## Keywords

density functional theory calculations, fusion structural materials, high-throughput screening

Received: June 19, 2022

Revised: August 7, 2022

Published online: September 30, 2022

- [1] J. Knaster, A. Moeslang, T. Muroga, *Nat. Phys.* **2016**, *12*, 424.
- [2] R. Gao, M. Jin, Q.-J. Li, K. P. So, L. Zhang, X. Wang, Q. Fang, C. Sun, L. Shao, J. u Li, *Scr. Mater.* **2021**, *194*, 113706.
- [3] M. R. Gilbert, S. L. Dudarev, S. Zheng, L. W. Packer, J.-C.h. Sublet, *Nucl. Fusion* **2012**, *52*, 083019.
- [4] F. R. N. Nabarro, *Proc. Phys. Soc.* **1940**, *52*, 90.
- [5] K. P. So, A. Kushima, J. G. Park, X. Liu, D. H. Keum, H. Y. Jeong, F. Yao, S. H. Joo, H. S. Kim, H. Kim, J. u Li, Y. H. Lee, *Adv. Sci.* **2018**, *5*, 1800115.
- [6] J. D. Whittenberger, *Metall. Trans. A* **1977**, *8*, 1155.
- [7] S. J. Zinkle, L. L. Snead, *Annu. Rev. Mater. Res.* **2014**, *44*, 241.
- [8] G. R. Odette, M. J. Alinger, B. D. Wirth, *Annu. Rev. Mater. Res.* **2008**, *38*, 471.
- [9] P. Song, D. Morrall, Z. Zhang, K. Yabuuchi, A. Kimura, *J. Nucl. Mater.* **2018**, *502*, 76.
- [10] L. L. Hsiung, M. J. Fluss, S. J. Tumej, B. W. Choi, Y. Serruys, F. Willaime, A. Kimura, *Phys. Rev. B – Condens. Matter Mater. Phys.* **2010**, *82*, 184103.
- [11] B. N. Sorbom, J. Ball, T. R. Palmer, F. J. Mangiarotti, J. M. Sierchio, P. Bonoli, C. Kasten, D. A. Sutherland, H. S. Barnard, C. B. Haakonsen, J. Goh, C. Sung, D. G. Whyte, *Fusion Eng. Des.* **2015**, *100*, 378.
- [12] K. P. So, D. i Chen, A. Kushima, M. Li, S. Kim, Y. Yang, Z. Wang, J. G. Park, Y. H. Lee, R. I. Gonzalez, M. Kiwi, E. M. Bringa, L. Shao, J. u Li, *Nano Energy* **2016**, *22*, 319.
- [13] K. P. So, X. Liu, H. Mori, A. Kushima, J. G. Park, H. S. Kim, S. Ogata, Y. H. Lee, J. u Li, *Extrem. Mech. Lett.* **2016**, *8*, 245.

- [14] P. Cao, K. P. So, Y. Yang, J. G. Park, M. Li, L. Yan, J. Hu, M. Kirk, M. Li, Y. H. Lee, M. P. Short, J. Li, *Acta Mater.* **2021**, *203*, 116483.
- [15] A. Jain, S. P. Ong, G. Hautier, W. Chen, W. D. Richards, S. Dacek, S. Cholia, D. Gunter, D. Skinner, G. Ceder, K. A. Persson, *APL Mater.* **2013**, *1*, 011002.
- [16] N. Kempf, M. Saeidi-Javash, H. Xu, S. Cheng, M. Dubey, Y. Wu, J. Daw, J. u Li, Y. Zhang, *Energy Convers. Manag.* **2022**, *268*, 115949.
- [17] P. Erhart, *J. Appl. Phys.* **2012**, *111*, 113502.
- [18] M. A. Tschoop, F. Gao, L. Yang, K. N. Solanki, *J. Appl. Phys.* **2014**, *115*, 033503.
- [19] D. H. Levy, *Adv. Chem. Physics, Photoselective Chem.* **2006**, 323.
- [20] S. Yip, *Nature* **1998**, *391*, 532.
- [21] S. Suresh, J. u Li, *Nature* **2008**, *456*, 716.
- [22] I. Levin, *NIST Inorganic Crystal Structure Database (ICSD)*, National Institute of Standards and Technology, Gaithersburg, MA **2018**.
- [23] M. R. Gilbert, M. Fleming, J.-C. Sublet, *Nucl. Eng. Technol.* **2017**, *49*, 1346.
- [24] E. J. Pickering, A. W. Carruthers, P. J. Barron, S. C. Middleburgh, D. E. J. Armstrong, A. S. Gandy, *Entropy* **2021**, *23*, 23010098.
- [25] J. G. Park, J.-G. Kim, K. P. So, J. Y. Hwang, E. S. Kim, J. u Li, D. Suh, Y. H. Lee, *Carbon N. Y.* **2019**, *153*, 513.
- [26] M. De Jong, W. Chen, T. Angsten, A. Jain, R. Notestine, A. Gamst, M. Sluiter, C. Krishna Ande, S. Van Der Zwaag, J. J. Plata, C. Toher, S. Curtarolo, G. Ceder, K. A. Persson, M. Asta, *Sci. Data* **2015**, *2*, 150009.
- [27] M. De Jong, W. Chen, R. Notestine, K. Persson, G. Ceder, A. Jain, M. Asta, A. Gamst, *Sci. Rep.* **2016**, *6*, 34256.
- [28] C. Sun, Y. Wang, M. D. Mcmurtrey, N. D. Jerred, F. Liou, J. u Li, *Appl. Energy* **2021**, *282*, 116041.
- [29] D. Morgan, G. Pilania, A. Couet, B. P. Uberuaga, C. Sun, J. u Li, *Curr. Opin. Solid State Mater. Sci.* **2022**, *26*, 100975.
- [30] S. Y. Kim, J. Li, *J. Mater.* **2022**, *8*, 195.
- [31] D. A. Porter, K. E. Easterling, *Phase transformations in metals and alloys*, CRC press, **2009**.
- [32] N. Qu, Y. Liu, M. Liao, Z. Lai, F. Zhou, P. Cui, T. Han, D. Yang, J. Zhu, *Ceram. Int.* **2019**, *45*, 18551.
- [33] E. W. Kammer, T. E. Pardue, H. F. Frissel, *J. Appl. Phys.* **1948**, *19*, 265.
- [34] D. Sun, P. Zhang, J. Ding, J. Zhao, *J. Nucl. Mater.* **2018**, *507*, 101.
- [35] S. Gorsse, C. Hutchinson, M. Gouné, R. Banerjee, *Sci. Technol. Adv. Mater.* **2017**, *18*, 584.
- [36] H. O. Pierson, *Handbook of refractory carbides and nitrides: properties, characteristics, processing and applications*, Noyes Publications, Park Ridge, NJ **1996**.
- [37] T. Timmerscheidt, P. Dey, D. Bogdanovski, J. Von Appen, T. Hickel, J. Neugebauer, R. Dronskowski, *Metals (Basel)*. **2017**, *7*, 264.
- [38] T. Voisin, Exploration de la voie SPS pour la fabrication d'aubes de turbine pour l'aéronautique: Développement d'un alliage TiAl performant et densification de préformes, Thesis, Université de Toulouse **2014**.
- [39] J. F. Ziegler, M. D. Ziegler, J. P. Biersack, *Nucl. Instrum. Methods Phys. Res., Sect. B: Beam Interact. Mater. Atoms* **2010**, *268*, 1818.
- [40] R. E. Stoller, M. B. Toloczko, G. S. Was, A. G. Certain, S. Dwaraknath, F. A. Garner, *Nucl. Instrum. Methods Phys. Res., Sect. B: Beam Interact. Mater. Atoms* **2013**, *310*, 75.
- [41] G. Kresse, J. Furthmuller, *Comput. Mater. Sci.* **1996**, *6*, 15.
- [42] W. Kohn, L. J. Sham, *Phys. Rev.* **1965**, *140*, A1133.
- [43] P. Hohenberg, W. Kohn, *Phys. Rev.* **1964**, *136*, B864.
- [44] J. P. Perdew, K. Burke, M. Ernzerhof, *Phys. Rev. Lett.* **1996**, *77*, 3865.
- [45] P. E. Blöchl, *Phys. Rev. B* **1994**, *50*, 17953.
- [46] A. Hjorth Larsen, J. Jorgen Mortensen, J. Blomqvist, I. E. Castelli, R. Christensen, M. Dulak, J. Friis, M. N. Groves, B. Hammer, C. Hargus, E. D. Hermes, P. C. Jennings, P. Bjerre Jensen, J. Kermode, J. R. Kitchin, E. Leonhard Kolsbjerg, J. Kubal, K. Kaasbjerg, S. Lysgaard, J. Bergmann Maronsson, T. Maxson, T. Olsen, L. Pastewka, A. Peterson, C. Rostgaard, J. Schiøtz, O. Schutt, M. Strange, K. S. Thygesen, et al., *J. Phys.: Condens. Matter* **2017**, *29*, 273002.